Research Article Vol. 32, No. 20 / 23 Sep 2024 / Optics Express 34314

Optics EXPRESS

Low-complexity turbulence resilience enabled by a multi-mode bi-directional transceiver

ULTAN J. DALY,[1] FORTUNE IGA,[2] ALEKSANDR BOLDIN,[1] ADAM J. VALLANCE,[1] MITCHELL A. COX,[2] AND MARTIN P. J. LAVERY[1,*]

[1] *James Watt School of Engineering, University of Glasgow, Glasgow, UK*
[2] *School of Electrical and Information Engineering, University of Witwatersrand, Johannesburg, South Africa*
[*] *martin.lavery@glasgow.ac.uk*

Abstract: Free-space optical (FSO) communication systems are acutely affected by the pointing issues and distortions that result from mechanical instability and environmental factors such as turbulence. These distortions have generally prevented single-mode bi-directional systems from being deployed without adaptive optics due to high optical losses. We investigate and compare the performance of both step and graded index multi-mode fibers for bi-directional communications over an emulated 400 m FSO channel. We propose that OM5 graded index fiber will simultaneously provide a near Gaussian optical transmission mode and a factor of greater than 5 increase in the field of view compared to single-mode fiber. We demonstrate that OM5 can support an error-free throughput of 10 Gbps for low-turbulence ($D/r_0 = 3$) and 9.1 Gbps for high-turbulence ($D/r_0 = 9$) using commercial bi-directional small form-factor pluggable (SFP+) transceivers with no adaptive optical components.

1. Introduction

Free-space optical (FSO) communication systems have the potential to provide high-speed wireless connections with reduced infrastructure requirements compared to fiber installation, making FSO a strong candidate for serving rural or developing communities [1,2]. However, FSO systems generally require complex tracking systems and adaptive optics to support high capacity communication channels due to environmental factors such as atmospheric turbulence or mechanical instability [3–7]. Atmospheric turbulence results from the continuous variation in temperature and pressure along a free-space path, which leads to changes in optical density resulting in time-dependent phase changes across the wavefront of an optical beam [8]. These distortions lead to an increased long-exposure point-spread function (PSF) at the back focal plane of a receiver lens [9,10], preventing effective coupling into single-mode (SM) optical fibers [11,12]. The short-exposure PSF changes continuously in reaction to the random phase fluctuations induced by the environment, which can produce deep-fades where there is sudden loss of received power, resulting in bit errors, a low signal to noise ratio (SNR), and packet loss [3,4,13].

SFP (small form-factor pluggable), SFP+ and QSFP (quad small form-factor pluggable), transceivers offer convenient high-speed (100 Mbps – 100 Gbps+) modulation with the ability to deal with high power penalties (>30 dB). The widespread availability of transceivers with the ability to tailor the data-rate and power budget to system requirements makes them ideal for low complexity FSO systems. However, they are commonly designed for use with SM fiber. SM fiber has a limited acceptance angle, which means that when used in an FSO system there is

#532749 https://doi.org/10.1364/OE.532749
Journal © 2024 Received 13 Jun 2024; revised 4 Aug 2024; accepted 21 Aug 2024; published 9 Sep 2024

generally a requirement for real-time adaptive optics to overcome the challenges of beam-wander and changes in the PSF at the receiver [14,15].

Mitigating the impact of turbulence in FSO systems has been an active research area with commonly considered techniques including spatial diversity schemes [16–18], MIMO digital signal processing [19,20] and integrated photonic receivers [21]. Passive approaches have also been considered, including fluorescent receivers [22,23], large area photodetectors [24], and wide field of view optics [25] among others. However, these schemes commonly require custom components not readily available for integration into deployable systems. FSO systems built upon widely-available commercial components, such as SFPs and industry standard optical fibers, could allow for the rapid and effective deployment of high-speed communication links. Multi-mode (MM) fibers offer an interesting alternative, as these have a larger acceptance angle and spatial bandwidth, allowing for the efficient coupling of a received beam with an aberrated PSF due to turbulence [11,13,26–32], as well as increased resilience to pointing errors [33–35]. Previous works typically utilize non-commercial transceivers for use with MM fiber. SFPs are specified for use with SM fiber, and are therefore not typically used for the reception of MM fibers. However, 10 Gbps SFPs use 20 GHz InGaAs photodiodes, which may have active areas with a diameter of >30 µm [36,37]. As the active areas are larger than SM Gaussian beams, the SM fiber filters more of the systems spatial bandwidth than the photodiode. This suggests using MM fiber for the reception of turbulent modes could improve the coupled power compared to the use of a SM fiber. Additionally, intermodal coupling within MM fibers is commonly considered to limit their usage as effective transmitters for FSO applications because the higher-order output field will be considerably more divergent than an equivalent field created by an SM fiber based transmitter.

In this work, we demonstrate the use of various industry standard MM fibers for both transmitting and receiving optical signals through turbulent FSO channels. We assessed the performance of a full FSO system design that uses MM fiber with commercially available SFPs, as depicted in Fig. 1. Utilising a computational simulation and measured optical fields from MM fibers, we analyzed the performance of these devices through representative thick turbulence environments, allowing us to assess full system performance. We systematically investigated the output mode quality of light coupled into short lengths (approx. 1 m) of OM1, OM2, OM3, OM4 and OM5 fiber, determining that OM1 and OM5 provide near Gaussian fields suitable for low-loss FSO transmission. A spatial light modulator (SLM) is then used to accurately recreate

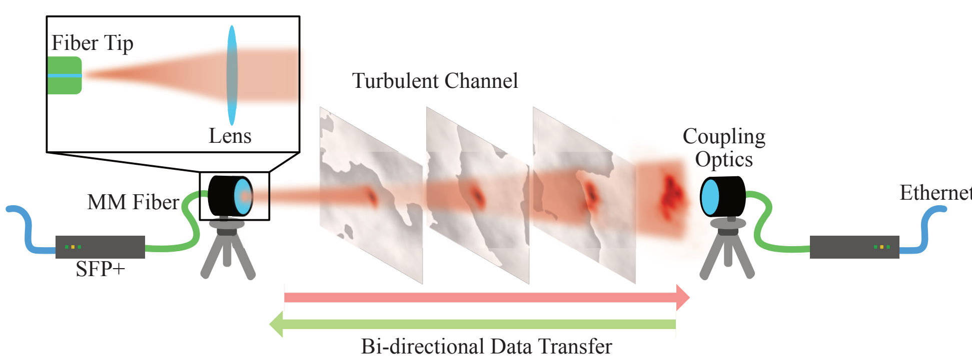

Fig. 1. The proposed system setup uses a bi-directional SFP+ connected to a short length of multi-mode fiber (MM fiber). As the beam propagates throughout the channel, it experiences phase and intensity aberrations that change the PSF, reducing coupling efficiency. In the proposed system the SFP is placed in the head unit of the FSO system to keep the MM fiber short to reduce intermodal coupling and minimize the impact of modal group delay.

the phase and intensity of the received optical fields in an experimental setup, and the fields are projected onto each MM fiber to assess their performance. Our experimental results confirm that using OM5 fiber in combination with a dual wavelength bi-directional SFP+, can achieve a sustained error-free throughput of 9.1 Gbps with a transmitted power margin of 8.6 dB for an emulated channel of at least 400 m with strong turbulence. This result demonstrates a novel reuse of widely available commercial components to construct a turbulence resilient FSO system built utilising graded-index MM fibers without active wavefront control.

2. Theory

2.1. Turbulence background

Atmospheric turbulence results in small variations in the air temperature throughout space. These variations result in spatial differences in the refractive index of the medium, which perturb the transverse phase profile of a propagating beam. From Kolmogorov turbulence theory, it can be shown that the structure function, $D_n(r)$, of the refractive index variations is given by

$$D_n(r) = \langle [n(\mathbf{r}_1) - n(\mathbf{r}_2)]^2 \rangle = C_n^2 r^{2/3} \tag{1}$$

where C_n^2 is the refractive index structure parameter, which defines the strength of the refractive index variations [38], and $n(\mathbf{r})$ is the refractive index at position $\mathbf{r}$. In Kolmogorov turbulence the structure function is homogenous and isotropic. Therefore, the structure function only depends on the separation between two points ($r = |\mathbf{r}_2 - \mathbf{r}_1|$) and not the absolute coordinates $\mathbf{r}_1$ and $\mathbf{r}_2$.

As a beam propagates through a channel the refractive index variations are accumulated. The phase distortions result in a long-exposure PSF that is broader than the non-turbulent PSF. A common parameter to characterize the effect of turbulence on the PSF is D/r_0, where D is the receiving lens diameter, and r_0 is the Fried parameter, which is a measure of the coherence length across the beam phase profile [9]. In the case of a channel with a constant C_n^2, the Fried parameter is given by the equation

$$r_0 = (0.423 k^2 C_n^2 L)^{-3/5} \tag{2}$$

where k is the wavenumber of the beam, and L is the propagation distance [39]. In the condition $D/r_0 \ll 1$, the system's PSF is diffraction limited, whereas if $D/r_0 \gg 1$ the system is limited by turbulence. This is an important consideration for coupling light into SM fiber, as turbulence results in less power overlapping with the area of the core, reducing the coupled power, as shown in Fig. 2. Conversely, the majority of the power for the high-turbulence situation is contained

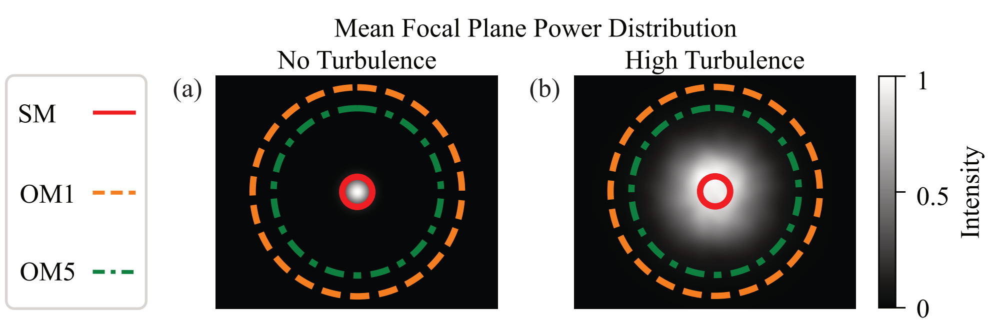

Fig. 2. The simulated long-time focal plane power distribution for a 75 mm diameter receiving lens with a focal length of 150 mm after a 400 m channel. (a) No turbulence throughout the channel. (b) A channel with a plane-wave $D/r_0 = 9$ (distribution from 500 realisations). The coloured circles represent the area covered by the core of SM, OM1, and OM5 fibers. The core diameters are 9 µm for SM, 50 µm for OM5, and 62.5 µm for OM5.

within the area of the MM fiber cores. The combination of increased core area, larger numerical aperture (NA), and increased spatial bandwidth, makes MM fibers significantly more resilient to turbulence aberrations compared to SM fibers.

As the beam propagates, the phase distortions give rise to interference that causes intensity fluctuations across the beam profile. The strength of the intensity fluctuations is given by the Rytov variance [38]

$$\sigma_R^2 = 1.229 C_n^2 k^{7/6} L^{11/6} \tag{3}$$

In the case that the channel is in the weak turbulence regime, where $\sigma_R^2 \ll 1$, the impact of turbulence can be modelled as a pure phase distortion. When $\sigma_R^2 > 1$, the channel is in the strong turbulence regime.

2.2. Clipping losses background

As a Gaussian beam propagates through a free-space channel, the beam radius will increase as the beam diffracts. Under non-turbulent conditions the beam radius at distance z from the beam waist, $w(z)$, can be calculated using the equation

$$w(z) = w_0 \sqrt{1 + \left(\frac{z}{z_\mathrm{R}}\right)^2} \tag{4}$$

where w_0 is the waist radius, and z_R is the Rayleigh length. The Rayleigh length is the distance at which the beam radius has increased by a factor of $\sqrt{2}$ with respect to the waist radius, and is given by the equation

$$z_\mathrm{R} = \frac{\pi w_0 n}{\lambda} \tag{5}$$

where n is the refractive index of the medium, and λ is the wavelength of the electromagnetic wave.

If the receiving aperture diameter, D, is comparable to or less than the beam diameter, $2w(z)$, there will be significant losses due to aperture clipping. By considering a Gaussian beam being clipped by a finite circular aperture it can be shown that the received power through a finite aperture, P_R, is given by

$$P_\mathrm{R} = P_0 \left(1 - \exp\left(\frac{-D^2}{2w(L)^2}\right)\right) \tag{6}$$

where P_0 is the total power of the unclipped Gaussian beam [40] is the beam waist given by Eq. (4) after propagation through the channel of length L.

When a Gaussian beam is propagated through atmospheric turbulence, there is an additional increase in the long-term beam radius at the receiver due to beam wander and beam spreading. The effective long-term beam radius at the receiving plane becomes [38]

$$w_e = w(L) \sqrt{1 + 1.63 \sigma_R^{6/5} \frac{2L}{k w(L)^2}}. \tag{7}$$

The effective beam radius w_e can be used in place of $w(z)$ in Eq. (6) to determine the mean clipping loss over long-time scales through a turbulent channel.

An additional factor in the aperture clipping is pointing accuracy. Misalignment and mechanical instability between the transmitting and receiving apertures will be associated with additional losses as the Gaussian is no longer centered on the receiving lens. By considering an off-centered

Optics EXPRESS

Gaussian over a circular aperture, we can determine that the power within the aperture is given by

$$P_R = P_0 \int_{-\rho}^{\rho} \int_{-\sqrt{\rho^2-y^2}}^{\sqrt{\rho^2-y^2}} \exp\left(-2\frac{(x+x_{off})^2+(y+y_{off})^2}{w_e^2}\right) dx\,dy \quad (8)$$

where $\rho = D/2$, and x_{off} and y_{off} are the Gaussian offset in the x and y coordinates, respectively. In the situation when $x_{off} = y_{off} = 0$, Eq. (8) simplifies to Eq. (6). In general, there is no analytical solution to Eq. (8), and values must be determined numerically [40].

When determining the received power for a fiber coupled system, Eq. (8) is valid under the assumption that aperture clipping is a more significant source of loss than focal plane coupling for a given pointing error. This assumption is not valid over short propagation lengths, as the loss due to pointing errors is associated with significant displacement in the focal plane and variations in the fiber-mode coupling [33–35]. However, when considering pointing errors over significant propagation lengths of hundreds or thousands of meters, the loss is dominated by the effect of aperture clipping rather than focal plane offset. This effect is due to the relatively small angular offset (<1 mrad) required to move the centre of mass of an optical field by tens of millimeters in the plane of the receiving optics.

The positional offset in the center-of-mass of the received Gaussian beam is given by $r_{off} = L \tan\theta$. Clearly, from this equation, the positional offset is dependent upon the propagation distance L and the pointing error θ. In contrast, the positional offset in the focal plane of a lens with a focal length f is given by $\Delta x = f \tan\theta$, which depends upon the pointing error, but not upon the propagation distance. For any given focal length, aperture diameter, and fiber core radius, a, there is some propagation length at which the received center-of-mass is clipped by the receiving aperture at a smaller pointing error than the associated focal point is clipped by the receiving fiber core. The condition required to meet this criterion is given by

$$L \geq \frac{fD}{2a}. \quad (9)$$

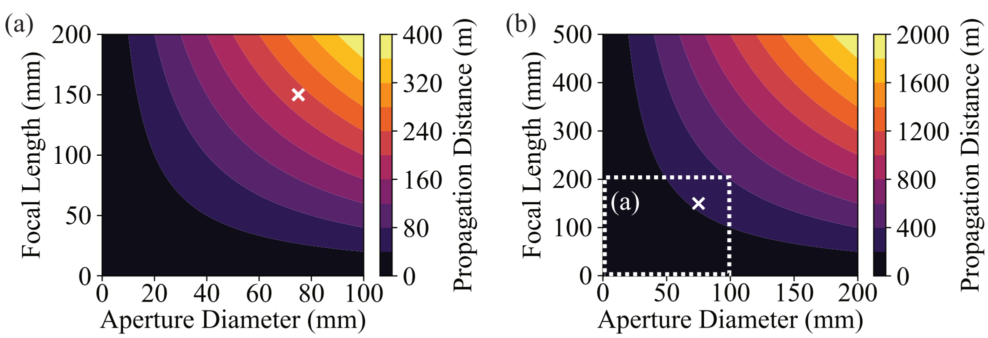

Fig. 3. For a fixed pointing error, the propagation distance of a channel increases the loss due to aperture clipping. This contrasts with the clipping due to changes in the focal plane center-of-mass, which depends on the pointing error, but is independent of the channel propagation distance. Depicted is the propagation distance required for the free-space Gaussian center-of-mass to reach the edge of the receiving aperture at a smaller pointing error than the focal plane center-of-mass reaches the edge of the fiber core for a 50 µm diameter core. The two plots (a) and (b) depict the results over different ranges of aperture diameter and focal length. The white cross indicates the parameters for the emulated system. The white box in (b) indicates the region covered in (a).

This is valid for MM fibers that couple well to the displaced Gaussian spots across the entire facet area, and in situations where the received beam has a focal point that covers a small portion of the fiber facet. Figure 3 depicts the minimum required propagation distance for Eq. (9) to be valid as a function of aperture diameter and focal length when $a = 25\,\mu$m.

3. Method

3.1. Fiber output field measurements

To simulate the performance of the MM fibers for bi-directional communication it was necessary to determine representative transmitted optical fields for each fiber. These representative transmitted fields were used as inputs for free space channel simulation concerning their respective fibers. The transmitted fields from OM1, OM2, OM3, OM4, and OM5 fibers were measured as the fibers were manipulated to give a wide range of possible intermodal coupling permutations. For these measurements, an SM fiber was used to couple light into the MM fibers.

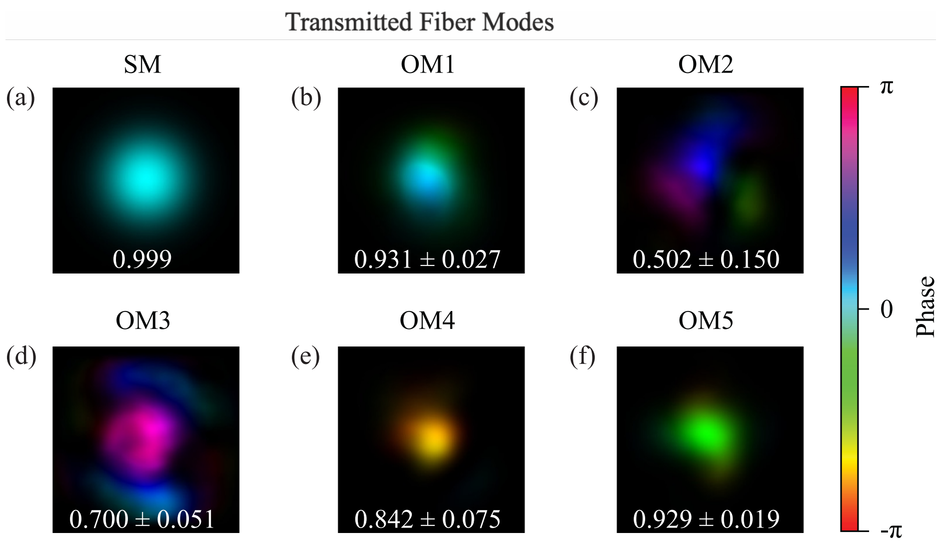

Fig. 4. Intensity and phase distributions of mean bandwidth modes measured from all observed fibers. Phase information is given by the color, and intensity information is given by the relative brightness. Inset in each image is the measured overlap to the best fit Gaussian mode from 100 realizations of the mean bandwidth mode.

SFP+ transceivers are specified for the power coupled into a connected SM fiber, assuming no fiber attenuation. When an SFP+ is directly coupled into an MM fiber, there is typically additional power coupled into higher-order fiber modes, but a power equivalent to the device specified power will couple into the same modes as the SM fiber. We would like to note that, in our experience, the multimode content of SFP transceivers varies quite significantly across manufacturers, and therefore so does the total output power of a connected MM fiber.

The length of all fibers was ≤ 1 m, and the field's phase and amplitude profiles were measured using off-axis digital holography [41] for nine separate bends along both orthogonal polarization axes for a total of 18 field realizations from each fiber. The captured fields for each fiber were decomposed using singular value decomposition (SVD) [42] to determine a set of singular modes that can decompose the transmitted field under all bends.

For each fiber, mean bandwidth modes were constructed of weighted singular modes with a random phase-offset, as shown in Fig. 4. The weightings of the singular modes were defined from their mean weighting across all measured field realizations. The mean bandwidth modes are representative of the mean field that is transmitted from the fibers under reasonable bending. To determine the fibers which have the best transmitter characteristics, the normalized overlap integral between 100 realizations of the mean bandwidth mode and a best-fit Gaussian was calculated. OM1 and OM5 were determined to have the highest Gaussian content (OM1: 0.931 ± 0.027, OM5: 0.929 ± 0.019), and were therefore the fibers used for further investigation.

3.2. Simulation

To determine beam fields after transmission through representative turbulent channels, a split-step propagation simulation was performed [39,43]. The phase screens for the simulated channel were generated using Fourier methods, enhanced with subharmonic sampling [44]. The simulation system emulated a deployed FSO system with 75 mm diameter transmitter and receiver apertures, both with a 150 mm focal length lens. The lens of the simulated system was chosen such that the NA of the lens (0.24) closely matched the NA of the MM fibers (OM1 = 0.275, OM5 = 0.2).

The beam waist of a collimated SM beam can be determined by using Eq. (4), where w_0 for an SM fiber field is 5.2 µm at the facet [45]. Using this information, and the measured best-fit Gaussian beam waists for the mean-bandwidth modes, the beam waist of all of the fibers after collimation by a 150 mm focal length lens can be determined. After collimation, the waists of the best fit Gaussian beams are 1.42 cm for SM, 1.21 cm for OM1, and 1.12 cm for OM5. These beam waists were used to expand the mean-bandwidth modes of OM1 and OM5 such that the simulated transmitted fields were representative of the fields that would be propagated from the transmitting lens.

Five hundred simulations were performed for nine different plane-wave turbulence strengths, $D/r_0 = \{1, 2, \ldots, 9\}$ over 400 m, which corresponds to a $C_n^2 = (2.70\times10^{-14}$ to $1.05\times10^{-12})\ \mathrm{m}^{-2/3}$, representing the turbulence expected over a real world terrestrial channel [46–48]. For each fiber a representative mean bandwidth mode, as determined from the SVD, was propagated through the same set of turbulence realizations.

It is known that the split-step propagation simulation using a single phase screen is only valid in the weak turbulence regime. From Eq. (3) it can be calculated that for the strongest investigated turbulence, $C_n^2 = 1.05 \times 10^{-12}\ \mathrm{m}^{-2/3}$, the associated Rytov variance is $\sigma_R^2 = 3.89$, and the single phase screen simulation does not produce accurate turbulent beam profiles. To ensure that the simulation is accurate across the full range of turbulence strengths for the propagation distance of 400 m we divided the simulation into ten propagation steps with ten phase screens [39], with each step having an equal C_n^2. This limits the largest Rytov variance of any step in our simulation to a value of $\sigma_R^2 = 0.06$, comfortably within the weak turbulence regime.

3.3. Experimental system

To experimentally replicate the received optical fields that resulted from the simulated propagation of the fiber fields through the turbulent channel, an SLM (Meadowlark HSP1920-850-1650) was used to shape the phase and intensity distribution of an incident optical field using first-order diffractive holography [49], as shown in Fig. 5. By using the SLM to accurately recreate phase-intensity profiles of the simulated fields, the system was enabled to model thick turbulence scenarios, which could not be performed if the SLM was used for phase-only modulation [50]. For our setup the system losses from the SLM diffraction grating and back reflections from the lenses was measured to be 2 dB. However, the efficiency of the SLM was highly dependent on the intensity modulation pattern associated with a beam profile, and did not correspond to the expected power coupled into the receiving aperture, as determined from the simulation results. To correct for this discrepancy, the power coupled out from the SLM was controlled by a variable optical attenuator (VOA) in the path of the illuminating fiber input. Some high-turbulence modes would have very poor coupling efficiency from the SLM. To experimentally explore a wide range of system power margins, an erbium-doped fiber amplifer (EDFA) is used such that up-to 17 dBm can illuminate the SLM. A 50:50 beamsplitter was used to sample half of the power onto a

Optics EXPRESS

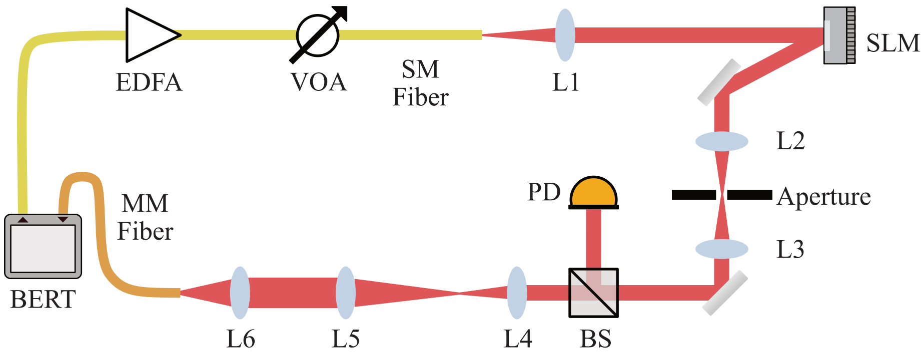

Fig. 5. Experimental setup of the system. An SFP+ connected to a bit error rate tester (BERT) transmits a 10 Gbps NRZ PRBS31 signal into a single-mode (SM) fiber. The power of the beam is controlled using an erbium-doped fiber amplifier (EDFA) and a variable optical attenuator (VOA), and the fiber output is collimated onto an SLM that generates the field produced by a pre-calculated turbulent mode. A beamsplitter (BS) is used to direct 50% of the power onto a photodiode (PD) for optical power measurements. The beam is expanded using a 2X magnifier (L4 - L5). The expanded beam is coupled into the multimode (MM) fiber under test using a 25 mm focal length lens (L6) with a 25 mm aperture. The fiber terminates in the BERT.

power-meter, and the VOA attenuated the power coupled out of the SLM such that it matched the power coupled into the aperture in the beam propagation simulation.

The output of the SLM illuminated a receiving lens which coupled light into the optical fiber under test. The initial simulation considered a receiving aperture diameter of 75 mm, which corresponded to a 6.25 mm modelled aperture at the SLM plane after downscaling by a factor of 12. The beam was then expanded by a factor of two, such that the simulated aperture illuminating the receiving lens was 12.5 mm in diameter. To keep the experimental system NA-matched to the simulated FSO system, the receiving lens in the experimental system had a focal length of 25 mm. The SLM was illuminated by a collimated SM fiber output connected to a 10 Gbps SFP+ (FS SFP-10GZR-55 80 km) in a bit-error rate tester (BERT), which uses a non-return-to-zero (NRZ) signal. NRZ modulation is better suited for free-space systems than return-to-zero modulation formats, as NRZ is capable of coping with dynamic variations in the system attenuation.

To ensure that the field distribution generated from the SLM was representative of the received simulated optical field, the intensity pattern generated from the SLM was measured using an InGaAs camera (Allied Vision Goldeye CL-008 TEC1) that was $4f$-relayed from the SLM (optical plane of PD in Fig. 5). A normalized overlap integral was performed between the measured and simulated intensity profiles for 30 realizations of each turbulence strength. As shown in Fig. 6, the generated intensity profiles consistently had over 90% overlap with the simulated turbulent modes across all values of D/r_0. The overlap decreases as the turbulence strength of the simulation increases, as the SLM cannot match the required spatial resolution of the highly turbulent modes. The overlap integral was measured to be independent of the simulated input fiber mode. These measurements indicate a potential 5.2 ± 2.4 % lower power coupling for high turbulence in real-world environments compared to the experimentally replicated channel, as the power lost from high-frequency components is redistributed amongst the unfiltered low-frequency components that are better coupled by the receiver.

To determine the data-rate for each turbulence realization, the power-corrected beam profile was coupled into an MM fiber through the receiving lens, and was terminated in the BERT. The BERT was used to measure two parameters: the total number of received bits, and the bit

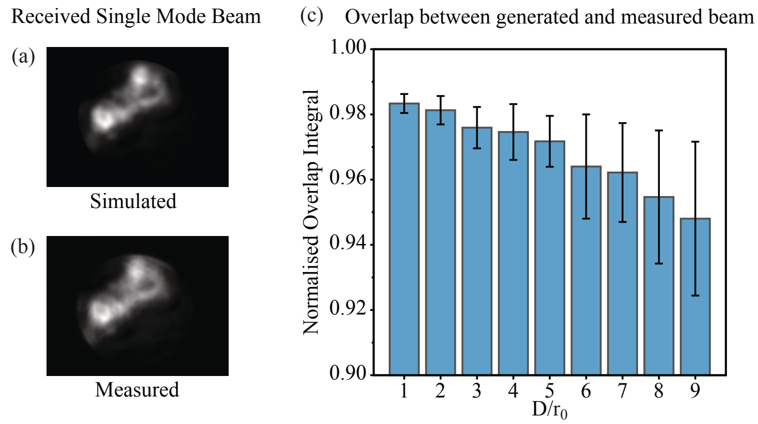

Fig. 6. (a) A simulated intensity profile of an SM beam transmitted through a 400 m turbulent channel with a $D/r_0 = 5$. (b) The experimental intensity profile of the beam simulated in (a), generated using the SLM. (c) Plots of the calculated overlap integral between the simulated beam profiles and the measured beam profiles generated using the SLM.

error rate (BER) of the received bits. These measurements were taken over a 3 s period for each turbulence realization.

In free-space optical communication systems, deep-fades due to atmospheric turbulence will result in burst errors as there is a significant drop in the SNR throughout the duration of the deep-fade. The deep-fade will have a duration comparable to the coherence time of turbulence, which is several orders of magnitude longer than the duration of a transmitted data-packet [51]. Networking solutions have been proposed that are designed to mitigate this issue by re-transmitting lost packets [13,52,53]. In these protocols the effect of deep-fades is a decrease in the system throughput, as multiple copies of the same packet may need to be transmitted. In this work we investigate the error-free throughput. This is calculated using the equation

$$R_{\mathrm{Eff}} = \left(\frac{b_{\mathrm{Rec}}}{b_{\mathrm{Trans}}} - \frac{b_{\mathrm{Err}}}{b_{\mathrm{Rec}}}\right) R_{\mathrm{Gross}} \tag{10}$$

where R_{Eff} is error-free throughput, R_{Gross} is the throughput of the SFP+, b_{Rec} is the total number of bits received, b_{Trans} is the total number of bits transmitted, and b_{Err} is the number of received errored bits.

4. Results

4.1. Measured channel throughput

Data is sent through the experimental system using a 10 Gbps NRZ SFP+ (FS SFP-10GZR-55 80 km) connected to a Viavi MTS-5800 BERT, which records the total number of received bits and the BER. The throughput of this system in a back-to-back configuration is measured to be 10.31 Gbps. From these two parameters, the error-free throughput is calculated using Eq. (10).

By using the VOA with an additional attenuation factor, the error-free throughput is measured as a function of the power margin with respect to the error-free noise-floor. The power margin is the transmitted power margin, not accounting for losses due to turbulence or beam clipping. The error-free noise floor is defined by the lowest power that achieves a BER = 0 over a 1000 s interval in a back-to-back configuration, and is measured as −24.6 dBm for the SFP used in this experiment. The investigated power margin covers the range of $\{-1.4, 0.6, \ldots, 14.6\}$ dB. The mean overlap integral between the generated and simulated beams shown in Fig. 6(c) is used to

Optics EXPRESS

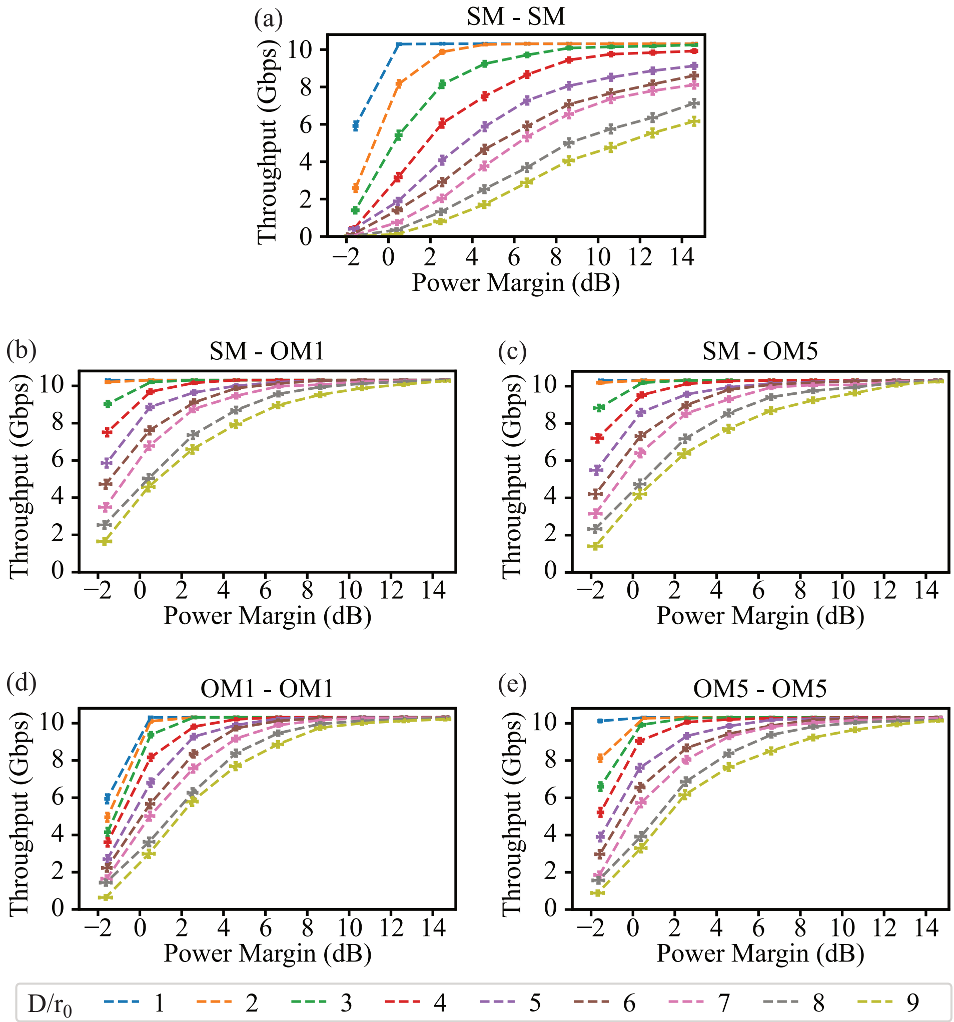

Fig. 7. The measured error-free throughput as a function of D/r_0 for a number of different transmitted power margins with respect to the error-free noise floor. The throughput of the system under ideal conditions is measured to be 10.31 Gbps.

determine an error in the measured power margin. Additionally, an error due to the difference between the targeted and measured input beam powers is accounted for in a change in the mean and error of the power margin values. The uncertainty in the throughput is due to the standard error of the mean.

4.2. Pointing error

As discussed in Sec. 2.2, a beam propagated through a free-space channel will experience losses due to pointing errors and beam divergence. Using Eqs. (6) and (9), the expected mean losses for the mean bandwidth modes of OM1 and OM5 are investigated.

Figure 8 depicts the clipping loss associated with propagating the collimated mean bandwidth modes from each fiber as a function of propagation length and D/r_0. The receiving and transmitting apertures have diameters of 75 mm, and the focal length of the transmitting lens is 150 mm. This results in a collimated input best fit Gaussian radius of 1.21 cm for OM1 and

Optics EXPRESS

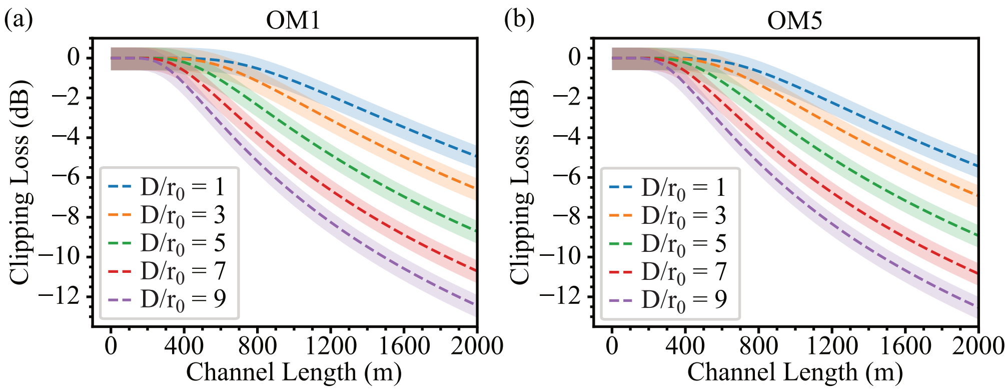

Fig. 8. The long-term mean loss due to diffraction induced losses of the mean bandwidth modes of each fiber for a system with a 75 mm diameter receiving aperture as a function of propagation distance. The input beams are collimated from the respective fibers using a 150 mm focal length lens. The confidence intervals are due to the fraction of power of the transmitted fiber mode that does not overlap with the best-fit Gaussian beam.

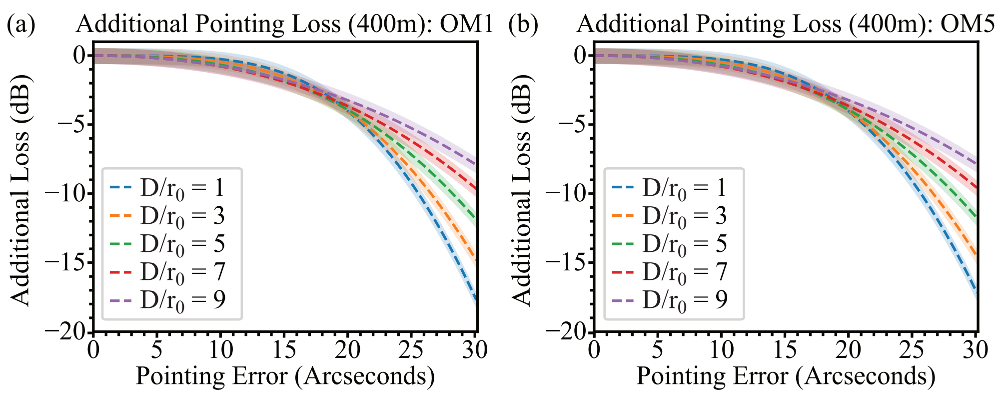

Fig. 9. The mean additional coupling loss from aperture clipping when the system is misaligned by some angular degree over a 400 m channel through different turbulence strengths. The results are shown for (a) propagation of OM1, (b) propagation of OM5. The confidence intervals are given by the the percentage of the power in the mean-bandwidth mode that does not overlap with the best-fit Gaussian mode.

1.12 cm for OM5. The clipping losses are calculated by determining the loss of the best fit Gaussian beam across the channel, and using the overlap integral to determine a confidence interval in the clipping loss.

In addition to the clipping loss due to diffraction there will also be losses associated with pointing errors. This additional loss, as calculated using Eq. (9), is depicted in Fig. 9 for both OM1 and OM5 mean bandwidth modes across a 400 m channel. To determine the total clipping loss for either fiber the values at 400 m from both Fig. 8 and 9 should be summed.

4.3. Impact of deep-fades and atmospheric coherence time

In addition to the losses during deep-fades there may be additional data-rate reductions due to reconnection times when power is reestablished between the SFPs. To determine the expected impact of this loss we define a reconnection loss factor that can be used to adjust the error-free throughput from Eq. (10). The reconnection loss factor is given by

$$A = \begin{cases} 1 - \frac{\tau_R}{\tau_c \times S_r} & \text{if} \tau_R \leq \tau_c \times S_r \\ 0 & \text{otherwise} \end{cases} \tag{11}$$

where τ_c is the coherence time of turbulence, τ_R is the SFP reconnection time, and S_r is the mean number of turbulence realizations between deep-fades. This calculation is made under the approximation that realizations separated by a time difference of τ_c can be treated as independent realizations of turbulence. From this assumption it can be deduced that the mean time between deep-fades is given by τ_c x S_r. Over prolonged time periods this factor can be used to correct the effective throughput in Eq. (10), such that the reconnection and coherence time adjusted throughput becomes $R_{\text{Coh}} = AR_{\text{Eff}}$.

SFP standards require loss of signal indicators to have a negation delay of less than 100 µs [54]. Coherence times of turbulence are typically in the range of 10 ms [55,56], which would result in a ratio of $\tau_c/\tau_R = 100$. However, in extreme conditions, coherence times approaching 1 ms may occur. For our device we measured a reconnection time of 3 ms. We consider the expected performance of our device for a coherence time of 10 ms, but additional considerations would be required for systems where the coherence time is expected to be shorter. Figure 10 shows the reconnection loss factor for a series of τ_c and τ_R ratios as a function of D/r_0 and different power margins for an OM5 - OM5 system.

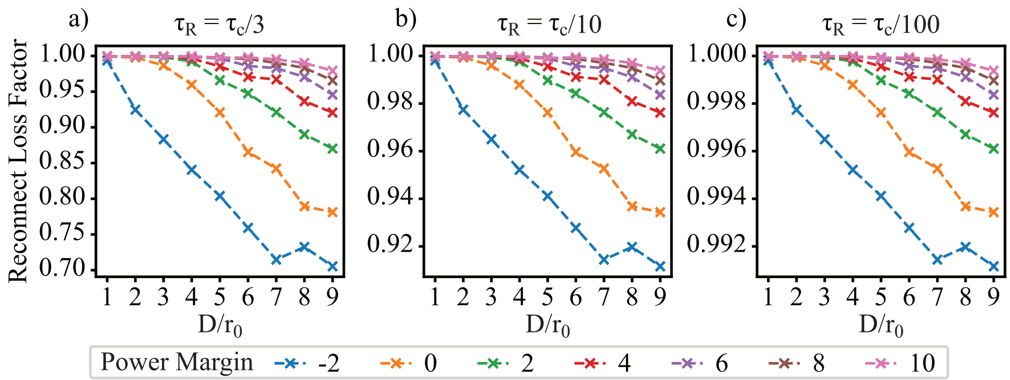

Fig. 10. The reconnect loss factor as a function of D/r_0 for OM5 - OM5. This factor accounts for SFP reconnection times following deep-fades, and the frequency of deep-fades to determine a correction factor for the expected throughput, R_{Eff} presented in Fig. 7 using the equation $R_{\text{Coh}} = AR_{\text{Eff}}$ a) $\tau_R = \tau_c/3$, b) $\tau_R = \tau_c/10$, c) $\tau_R = \tau_c/100$.

5. Discussion

From the results shown in Fig. 7, it has been shown that a simplex system comprising an SM transmitter and an OM1 receiving fiber has the highest sustained error-free throughput across all measured transmitted power margins. The increased performance of the MM receiving fibers over the SM receiving fiber demonstrates that the SFP photodiode couples into more of the received MM field than the SM component (see supplementary). The benefit of using OM1 for the receiving fiber over OM5 for the same transmitted SM beam can be attributed to the larger NA of OM1 fiber. However, in a bi-directional configuration, OM5 maintains a higher error-free throughput than OM1 for a transmitted power margin of ≤ 1.7dB across all measured turbulence strengths. This suggests that OM5 has superior transmission properties compared to OM1 for use in a bi-directional system. When comparing a simplex and bi-directional OM5

Optics EXPRESS

system, there is a 36 % throughput reduction at $D/r_0 = 9$ and power margin of -1.6 dB, as shown in Fig. 7. The higher spatial bandwidth of the transmitted OM5 beam compared to the SM beam reduces the coupling efficiency through turbulent channels as expected. However, for higher power margins the throughput penalty from using an OM5 bi-directional system over a simplex system reduces, with less than a 2 % reduction in throughput at $D/r_0 = 9$ and power margin of 14.6 dB. In turbulent conditions, a bi-directional SM system has the worst error-free throughput across all investigated power margins, as is to be expected due to the increase in the PSF.

Fig. 10 demonstrates that the reconnection loss factor is small for high power margins, and when the reconnection time is significantly shorter than the average time between deep-fades. The reconnection time of SFPs could be as small as 100 µs, which is significantly shorter than typical atmospheric coherence times. However, this must be considered when designing the FSO system if there is expected to be a significant proportion of deep fades.

Figure 8 demonstrates that, for a 400 m channel, there are no significant diffraction related losses across all turbulence strengths. However, this figure only analyzes the mean losses. As the mean losses increase with turbulence, it can be deduced that the increase in loss is associated with beam-wander, and is likely to result in deep-fades. The diffraction related losses increase with propagation distance, with significant losses only occurring above 400 m. These increases can be mitigated by increasing the receiving aperture size accordingly, whilst also changing the focal length to keep an NA match between the MM fibers and the lens system.

Figure 9 suggests that higher turbulence strengths are less sensitive to pointing misalignments. This can be understood by considering Eq. (9), which demonstrates that a larger turbulence strength will have a larger long-term received beam radius. Due to the beam wandering, a system that is misaligned in a non-turbulent environment may ‘wander’ into alignment in turbulent situations, resulting in a higher effective throughput.

Both Figs. 8 and 9 investigate the mean coupling losses through the turbulent channel, and the instantaneous loss may significantly exceed the presented values, particularly in highly turbulent environments. However, the proposed packet transmission system is designed to cope with prolonged burst errors associated with turbulence induced deep-fades. It is therefore a reasonable approximation to assume that the mean reduction in the received power will be associated with a reduction in the power margin of the system, reducing the throughput in accordance with Fig. 7.

In addition to turbulence and clipping induced losses, there will also be losses due to atmospheric attenuation, which are highly dependent on visibility conditions and optical wavelength [4,57,58]. Using expected losses due to clipping and atmospheric attenuation, an expected power margin through the channel can be determined. Using Fig. 7, this power margin can be used to determine an expected system throughput for different levels of turbulence, under the assumption that Eq. (9) is true.

In this work, the transmitted mean bandwidth modes from the MM fibers are determined using an SM fiber input. When coupled to an SFP+ laser, there is likely to be additional coupling into higher-order modes within the MM fiber. However, SFP+ devices are rated by the power coupled into a SM fiber. This SM coupling portion of the SFP+ output will couple into the MM fiber and experience intermodal coupling equivalent to the intermodal investigated in Sec. 3.1. The additional power coupled into higher-order modes of the MM fiber will not reduce this low-order coupling power transmitted by the fiber. However, there is a possibility that it may increase the power received through the turbulent channel, as some of the additional coupled power may increase the power in low-order modal components of the MM fiber. This suggests that the performance demonstrated if Figs. 7(c)–(d) may actually improve, as there are additional transmitted field components that have not been accounted for in this work.

From this work it has been demonstrated that using OM5 fibers for bi-directional communication will result in a data-rate of ≥ 9.1 Gbps over the 400 m channel across all measured turbulence strengths with an assumption of an optical alignment error of 20 arcseconds and a transmitted power margin of ≥ 14.8 dB above the system error-free noise floor. The system is designed to have a short length of MM fiber between the optical system and the SFP to reduce intermodal coupling and the impact of modal group delay. The loss due to pointing errors has been analyzed, and can be used to determine the appropriate level of mechanical tracking required for real world system deployment.

By accounting for changes in the clipping loss and alignment error, as presented in this work, the Fried parameter of the channel can be used to determine reasonable performance expectations of the system at longer distances. For instance, using Eqs. (7) and (9), it can be determined that for a 1 km channel with $D/r_0 = 9$ and a pointing error of 20 arcseconds the expected loss due to aperture clipping in the proposed system is 12.8 dB. As variations in the fiber coupling are dominated by the Fried parameter, this value can be used to determine an expected throughput for a provided power margin using Fig. 7(e). A transmitted power margin of 14.8 dB would result in a received power margin of 2 dB (neglecting atmospheric attenuation which can be included as an additive loss), which translates to a received throughput of approximately 5 Gbps.

6. Conclusion

In this paper we show that graded index multi-mode fibers can be used as a method to provide increased turbulence resilience for a bi-directional FSO communication system utilizing SFP+ transceivers. It is observed that for an accurately aligned system with a transmitted power margin of 8.6 dB above the error-free noise floor the measured error-free throughput drops from 10 Gbps to 9.1 Gbps for a channel with $D/r_0 = 9$. The impact of pointing errors on the power margin requirements has also been considered. We have demonstrated that in the proposed configuration pointing error of 20 arcseconds results in an additional power penalty of 4 dB over a 400 m channel. We believe these findings will support the development of future low-complexity FSO communication systems.

7. Supplementary information

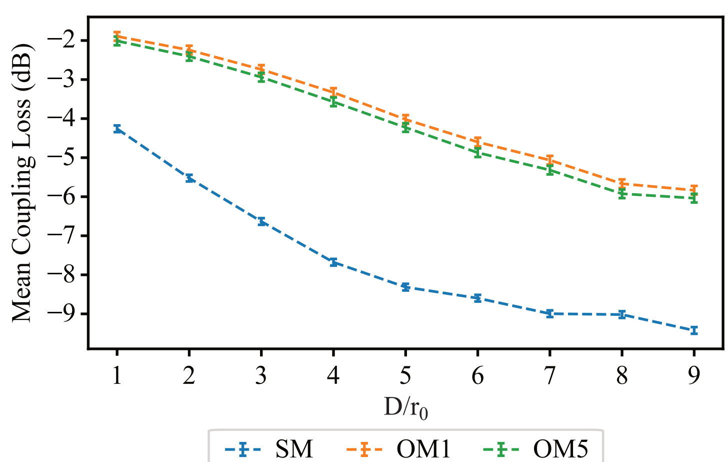

Fig. 11. The mean coupling loss between the power in the aperture and the power measured on the SFP as a function of the measured turbulence strength. The errorbars represent the standard error of the mean.

The use of SFPs designed for SM coupling for improved coupling is reliant on the photodiode capturing light with a higher spatial bandwidth than the SM fiber. Figure 11 presents the measured mean coupling loss between the power in aperture and the measured SFP received

Optics EXPRESS

power as a function of turbulence for SM, OM1, and OM5 fibers. SM fiber is significantly below both MM fibers, which can be interpreted as the SM fiber limiting the spatial bandwidth of the system more than the photodiode width. This is justified by the widespread availabilty of 20 GHz photodiodes with active area diameters >30 μm, significantly larger than a SM core. For modes with significant coupling losses the SFP does not provide accurate power readings, which may result in an underestimation of the coupling loss at high turbulence strengths.

Funding. Engineering and Physical Sciences Research Council (EP/S022821/1, EP/T009012/1); Royal Academy of Engineering (Transforming Systems through Partnership); National Research Foundation.

Acknowledgments. All authors thank Andrew Lord and Emilio Hugo Salas for useful conversations.

Disclosures. The authors declare no conflicts of interest.

Authors Contributions. The concept was developed by Martin P. J. Lavery and Mitchell A. Cox. The experimental approach was developed by Martin P. J. Lavery, Mitchell A. Cox, Ultan J. Daly, and Fortune Iga. The experimental measurements were conducted by Ultan J. Daly and Fortune Iga. The simulation was developed and conducted by Ultan J. Daly. The data presented in the manuscript was processed by Ultan J. Daly. Aleksandr Boldin assisted with the data processing and experimental measurements. Adam J. Vallance supported the experimental measurements. The manuscript was compiled by Ultan J. Daly and Martin P. J. Lavery. All authors have read and approved the manuscript.

Data availability. Data underlying the results presented in this paper are not publicly available at this time but may be obtained from the authors upon reasonable request.

References

1. M. P. Lavery, M. M. Abadi, R. Bauer, *et al.*, "Tackling Africa's digital divide," Nat. Photonics **12**(5), 249–252 (2018).
2. M. A. Imran, M. Zennaro, O. R. Popoola, *et al.*, "Exploring the boundaries of connected systems: communications for hard-to-reach areas and extreme conditions," Proceedings of the IEEE **in press** (2024).
3. E. Ciaramella, Y. Arimoto, G. Contestabile, *et al.*, "1.28 terabit/s (32x40 Gbit/s) wdm transmission system for free space optical communications," IEEE J. Select. Areas Commun. **27**(9), 1639–1645 (2009).
4. A. Trichili, M. A. Cox, B. S. Ooi, *et al.*, "Roadmap to free space optics," J. Opt. Soc. Am. B **37**(11), A184–A201 (2020).
5. M. M. Abadi, M. A. Cox, R. E. Alsaigh, *et al.*, "A space division multiplexed free-space-optical communication system that can auto-locate and fully self align with a remote transceiver," Sci. Rep. **9**(1), 19687 (2019).
6. Y. Kaymak, R. Rojas-Cessa, J. Feng, *et al.*, "A survey on acquisition, tracking, and pointing mechanisms for mobile free-space optical communications," IEEE Commun. Surv. Tutorials **20**(2), 1104–1123 (2018).
7. M. M. Freitas, M. A. Fernandes, P. P. Monteiro, *et al.*, "Requirements and solutions for robust beam alignment in fiber-coupled free-space optical systems," Photonics **10**(4), 394 (2023).
8. V. I. Tatarskii, *The Effects of the Turbulent Atmosphere on Wave Propagation* (trans. for NOAA by Israel Program for Scientific Translations, Jerusalem, 1971).
9. D. L. Fried, "Optical resolution through a randomly inhomogeneous medium for very long and very short exposures," J. Opt. Soc. Am. **56**(10), 1372–1379 (1966).
10. A. Glindemann, "Beating the seeing limit – adaptive optics on large telescopes," Habilitationsschrift, Universität Heidelberg (1997).
11. P. J. Winzer and W. R. Leeb, "Fiber coupling efficiency for random light and its applications to lidar," Opt. Lett. **23**(13), 986 (1998).
12. Y. Dikmelik and F. M. Davidson, "Fiber-coupling efficiency for free-space optical communication through atmospheric turbulence," Appl. Opt. **44**(23), 4946–4952 (2005).
13. L. B. Stotts, L. C. Andrews, P. C. Cherry, *et al.*, "Hybrid optical RF airborne communications," Proc. IEEE **97**(6), 1109–1127 (2009).
14. B. M. Levine, E. A. Martinsen, A. Wirth, *et al.*, "Horizontal line-of-sight turbulence over near-ground paths and implications for adaptive optics corrections in laser communications," Appl. Opt. **37**(21), 4553 (1998).
15. R. K. Tyson, D. E. Canning, and J. S. Tharp, "Measurement of the bit-error rate of an adaptive optics, free-space laser communications system, part 1: Tip-tilt configuration, diagnostics, and closed-loop results," Opt. Eng. **44**(9), 096002 (2005).
16. I. I. Kim, H. Hakakha, P. Adhikari, *et al.*, "Scintillation reduction using multiple transmitters," in *Photonics West '97*, G. S. Mecherle, ed. (San Jose, CA, 1997), pp. 102–113.
17. E. Shin and V. Chan, "Optical communication over the turbulent atmospheric channel using spatial diversity," in *Global Telecommunications Conference, 2002. GLOBECOM '02. IEEE*, vol. 3 (IEEE, Taipei, Taiwan, 2002), pp. 2055–2060.
18. M. A. Cox, L. Cheng, C. Rosales-Guzmán, *et al.*, "Modal diversity for robust free-space optical communications," Phys. Rev. Appl. **10**(2), 024020 (2018).
19. H. Huang, Y. Cao, G. Xie, *et al.*, "Crosstalk mitigation in a free-space orbital angular momentum multiplexed communication link using 4×4 MIMO equalization," Opt. Lett. **39**(15), 4360 (2014).

Optics EXPRESS

20. Y. Li, Z. Chen, Z. Hu, *et al.*, "Enhanced Atmospheric Turbulence Resiliency With Successive Interference Cancellation DSP in Mode Division Multiplexing Free-Space Optical Links," J. Lightwave Technol. **40**(24), 7769–7778 (2022).
21. G. Labroille, B. Denolle, P. Jian, *et al.*, "Efficient and mode selective spatial mode multiplexer based on multi-plane light conversion," Opt. Express **22**(13), 15599 (2014).
22. P. P. Manousiadis, S. Rajbhandari, R. Mulyawan, *et al.*, "Wide field-of-view fluorescent antenna for visible light communications beyond the étendue limit," Optica **3**(7), 702 (2016).
23. W. Ali, P. P. Manousiadis, D. C. OaBrien, *et al.*, "A gigabit VLC receiver that incorporates a fluorescent antenna and a SiPM," J. Lightwave Technol. **40**(16), 5369–5375 (2022).
24. Z. Wang, D. Tsonev, S. Videv, *et al.*, "On the design of a solar-panel receiver for optical wireless communications with simultaneous energy harvesting," IEEE J. Select. Areas Commun. **33**(8), 1612–1623 (2015).
25. O. Alkhazragi, A. Trichili, I. Ashry, *et al.*, "Wide-field-of-view optical detectors using fused fiber-optic tapers," Opt. Lett. **46**(8), 1916 (2021).
26. Y. Huang, H. Huang, H. Chen, *et al.*, "Free-space optics communications employing elliptical-aperture multimode diversity reception under anisotropic turbulence," J. Lightwave Technol. **40**(5), 1502–1508 (2022).
27. N. Fontaine, R. Ryf, Z. Yuanhang, *et al.*, "Digital turbulence compensation of free space optical link with multimode optical amplifier," in *45th European Conference on Optical Communication (ECOC 2019)*, (Institution of Engineering and Technology, Dublin, Ireland, 2019), p. 281.
28. H. Liu, B. Huang, J. C. A. Zacarias, *et al.*, "Turbulence-resistant FSO communication using a few-mode pre-amplified receiver," Sci. Rep. **9**(1), 16247 (2019).
29. S. Arisa, Y. Takayama, H. Endo, *et al.*, "Coupling efficiency of laser beam to multimode fiber for free space optical communication," in *International Conference on Space Optics — ICSO 2014*, B. Cugny, Z. Sodnik, and N. Karafolas, eds. (SPIE, Tenerife, Canary Islands, Spain, 2017), p. 162.
30. D. Zheng, Y. Li, E. Chen, *et al.*, "Free-space to few-mode-fiber coupling under atmospheric turbulence," Opt. Express **24**(16), 18739 (2016).
31. P. V. Trinh, D. R. Kolev, K. Shiratama, *et al.*, "Experimental verification of fiber coupling characteristics for FSO downlinks from the International Space Station," Opt. Express **31**(5), 9081 (2023).
32. V. D. Correia, M. A. Fernandes, P. P. Monteiro, *et al.*, "On the impact and mitigation of turbulence in fiber-coupled FSO systems," IEEE Access **12**, 69505–69516 (2024).
33. M. M. Freitas, M. A. Fernandes, P. A. Loureiro, *et al.*, "Robust and cost-efficient FSO transmission using a multi-mode fiber-coupled receiver," Opt. Continuum **3**(2), 227 (2024).
34. S. A. Tedder, B. Schoenholz, and S. N. Suddath, "Study of lateral misalignment tolerance of a symmetric free-space optical link for intra international space station communication," in *AIAA International Communications Satellite Systems Conference*, vol. 34th (2016).
35. B. L. Schoenholz, S. A. Tedder, P. Millican, *et al.*, "Bit error rate performance on passive alignment in free space optical links using large core fibers," in *Free-Space Laser Communication and Atmospheric Propagation XXX*, H. Hemmati and D. M. Boroson, eds. (SPIE, San Francisco, United States, 2018), p. 42.
36. Lumentum, *Avalanche Photodiode (APD) 10G Chip Datasheet* (2024). https://www.lumentum.com/en/products/avalanche-photodiode-10g-chip-PA006700.
37. Albis, *APD10D1 Datasheet* (2024). https://www.albisopto.com/albis_product/apd10d1-10-gb-s-apd-with-integrated-lens/.
38. L. C. Andrews and R. L. Phillips, *Laser Beam Propagation through Random Media* (SPIE Press, Bellingham, Wash, 2005), 2nd ed.
39. J. D. Schmidt, *Numerical Simulation of Optical Wave Propagation with Examples in MATLAB* (SPIE, 2010).
40. N. R. Barbeau, "Power deposited by a Gaussian beam on a decentered circular aperture," Appl. Opt. **34**(28), 6443 (1995).
41. J. Carpenter, "digHolo : High-speed library for off-axis digital holography and Hermite-Gaussian decomposition," in *Digital Holography and 3-D Imaging*, (Optica Publishing Group, 2022).
42. D. A. B. Miller, "Waves, modes, communications, and optics: A tutorial," Adv. Opt. Photon. **11**(3), 679–825 (2019).
43. M. P. Lavery, "Vortex instability in turbulent free-space propagation," New J. Phys. **20**(4), 043023 (2018).
44. R. G. Lane, A. Glindemann, and J. C. Dainty, "Simulation of a Kolmogorov phase screen," Waves Random Media **2**(3), 209–224 (1992).
45. Thorlabs, *SMF-28-J9 Datasheet* (2024). https://www.thorlabs.com/thorproduct.cfm?partnumber=SMF-28-J9.
46. A. Tunick, H. Rachele, F. V. Hansen, *et al.*, "REBAL '92—A cooperative radiation and energy balance field study for imagery and electromagnetic propagation," Bull. Am. Meteorol. Soc. **75**(3), 421–430 (1994).
47. A. Tunick, N. Tikhonov, M. Vorontsov, *et al.*, "Characterization of optical turbulence (Cn2) data measured at the ARL A_LOT facility," Technical Report, U.S. Army Research Laboratory Adelphi United States (2005).
48. L. B. Stotts, P. Kolodzy, A. Pike, *et al.*, "Free-space optical communications link budget estimation," Appl. Opt. **49**(28), 5333 (2010).
49. T. W. Clark, R. F. Offer, S. Franke-Arnold, *et al.*, "Comparison of beam generation techniques using a phase only spatial light modulator," Opt. Express **24**(6), 6249 (2016).
50. B. Rodenburg, M. Mirhosseini, M. Malik, *et al.*, "Simulating thick atmospheric turbulence in the lab with application to orbital angular momentum communication," New J. Phys. **16**, 1 (2014).
51. J. Davis and W. Tango, "Measurement of the atmospheric coherence time," PASP **108**, 456 (1996).

Optics EXPRESS

52. K. Kiasaleh, "Hybrid ARQ for FSO communications through turbulent atmosphere," IEEE Commun. Lett. **14**(9), 866–868 (2010).
53. Y. Hasegawa, "A transmission control protocol for free-space optical communications," in *GLOBECOM 2017 - 2017 IEEE Global Communications Conference*, (IEEE, Singapore, 2017), pp. 1–7.
54. SNIA, *SFF-8431 - SFP+ 10 Gb/s and Low Speed Electrical Interface* (2014). https://www.snia.org/technology-communities/sff/specifications.
55. J. Zhao, Y. Zhou, B. Braverman, *et al.*, "Performance of real-time adaptive optics compensation in a turbulent channel with high-dimensional spatial-mode encoding," Optics Express **28**, 15376–15391 (2020).
56. T. Weyrauch and M. A. Vorontsov, "Free-space laser communications with adaptive optics: Atmospheric compensation experiments," J Optic Comm Rep **1**(4), 355–379 (2004).
57. I. I. Kim, B. McArthur, and E. J. Korevaar, "Comparison of laser beam propagation at 785 nm and 1550 nm in fog and haze for optical wireless communications," in *Information Technologies 2000*, E. J. Korevaar, ed. (Boston, MA, 2001), pp. 26–37.
58. R. M. Pierce, J. Ramaprasad, and E. C. Eisenberg, "Optical attenuation in fog and clouds," in *ITCom 2001: International Symposium on the Convergence of IT and Communications*, E. J. Korevaar, ed. (Denver, CO, 2001), p. 58.